H-TYPE LINAC STRUCTURES

U. Ratzinger[*]
GSI Darmstadt, Darmstadt, Germany

Abstract

H-type cavities have been successfully developed over the last 25 years to serve for a large variety of applications in the field of ion acceleration. Radio Frequency Quadrupole (RFQ) and Drift Tube Linac (DTL) versions were designed in the H_{11}- as well as in the H_{21}-mode. The Interdigital H-type (IH) drift tube structure ($H_{11(0)}$-mode) is efficient for an energy range from 100 keV/u to 30 MeV/u, especially when combined with KONUS beam dynamics. In overall power consumption the IH-DTL can compete with existing superconducting linacs up to beam energies of around 2 MeV/u. Additionally, effective voltage gains as high as 10.7 MV/m were demonstrated in pulsed operation. The GSI High Current Linac has reached new marks for drift tube structures with $(A/q)_{max} \approx 60$ and $I_{max}/emA = 0.25 \cdot A/q$. The effective voltage gain of that 36 MHz, 80 MV IH-linac is 4.2 MV/m. The IH-RFQ (H_{110}-mode) is well suited for heavy-ion beams with $A/q \geq 10$, and the four-vane RFQ is very well established for proton and light-ion acceleration. At beam energies between 5 MeV/u and 150 MeV/u the Cross Bar H-Type (CH) drift tube structure (H_{210}-mode) also shows great potential for room temperature and for superconducting designs.

1. INTRODUCTION

H-type cavities are characterized by the direction of the RF magnetic field, which is parallel and anti-parallel with respect to the beam axis. Closed field loops are provided by connecting field lines with opposite orientation at the cavity ends.

At present RFQ and DTL versions exist for the H_{110}-mode as well as for the H_{210}-mode (Fig. 1). The Interdigital H-type drift tube structure (IH, H_{110}-mode) was mentioned as an attractive solution for proton acceleration up to 30 MeV at the 1956 CERN Symposium by J.P. Blewett [1]. Several groups have studied the capabilities of this structure [2–5] and important improvements and innovations were achieved during the design phase of many H-linac projects [6–12], including the RFQ developments at the very beginning. H-type cavities are characterized by a high capacitive load contribution of the accelerating electrodes that provide the longitudinal electric field components for beam acceleration. To minimize the electric capacitance of H-DTLs, KONUS beam dynamics was developed [11–14]. These allow the design of lens-free multigap sections transversally matched by quadrupole triplet lenses.

This article will describe a simple analytical approach suited to estimate the RF field distribution and the main geometrical and RF parameters of H-cavities. Necessary input parameters result from beam simulations using codes like PARMTEQ for RFQs and LORASR for H-DTLs. These codes allow the design of the accelerating electrodes that dominate the capacitive load of the cavities. Fairly exact cavity designs for an IH-RFQ [15] as well as complex IH-DTL cavities resulted from RF

[*] New address: IAP, J.W. Goethe-Universität, Robert-Mayer-Str. 2-4, 60325 Frankfurt, Germany

field calculations with MAFIA [16, 17]. In the latter case additional investigations of RF models were very helpful. Several aspects and details of IH-RFQs and of IH- and CH-DTLs are discussed.

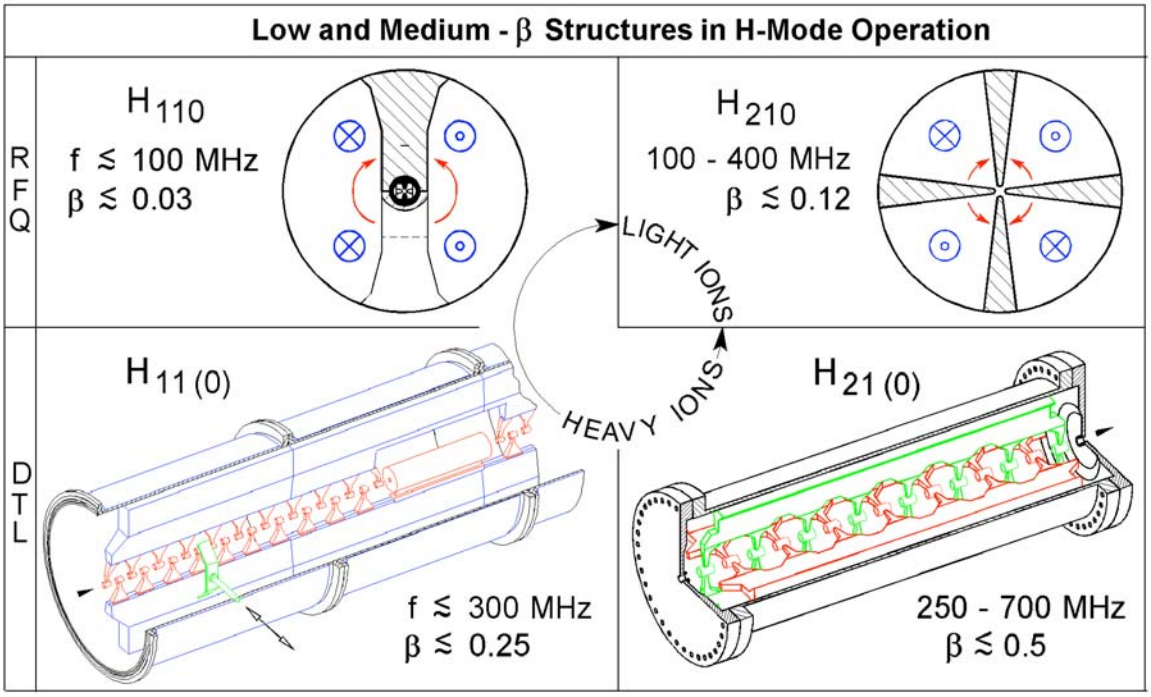

Fig. 1: H-type structure family

2. ANALYTICAL APPROACH TOWARDS H-TYPE CAVITIES

As E-modes by definition provide a dominant E-field component parallel to the beam axis, most accelerator cavities are related to that mode family. At beam velocities $\beta \lesssim 0.5$, however, H-mode cavities as shown in Fig. 1 provide excellent capabilities for ion acceleration. In RFQs the transverse electric quadrupole field components dominate, therefore the choice of H-modes is natural. For H-DTLs a number of developments were necessary to reach the present state of the art in terms of efficiency, ion current, beam quality, and reliability. Some effort is necessary to compute the characteristic parameters of H-structures. For the IH-DTL [18, 19] as well as for the four-vane RFQ [20] lumped circuit-based models were derived beforehand.

In this Section, a simplified model of the electromagnetic field distribution in H-cavities is described [14]. This allows the deduction of formulas for the estimation of all geometric and RF parameters. Optimization concepts can be deduced from these equations. Final cavity layouts, however, should be based on RF model measurements and on numerical field calculations with three-dimensional codes like MAFIA.

2.1 Field distribution

H-type accelerator structures are characterized by a very high capacitive load when compared with the corresponding mode in an empty cylindrical cavity. For example, the 202 MHz cavity shown in Fig. 2 has an averaged cavity diameter of 335 mm and length of 1.42 m. The $H_{1,1,1}$-mode of the corresponding empty cylinder has a resonance frequency of 535.3 MHz! The situation is quite different for Alvarez cavities (E_{010}-mode), where the resonance frequency of the empty cylinder is only reduced by

5–10% when inserting the drift tube structure. The frequency in H-type RFQs is degraded by factors of five (four-vane RFQ) to six (IH-RFQ) when inserting the structure.

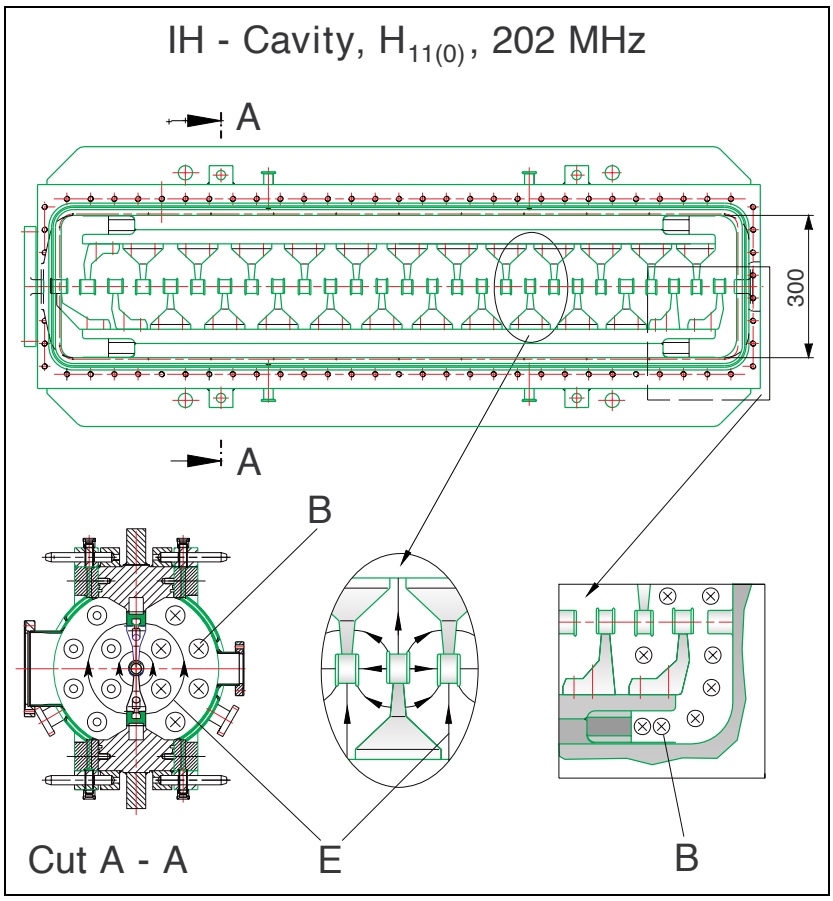

Fig. 2: Top: view of the 202 MHz drift tube structure of the CERN Pb^{25+} IH-DTL, tank 2. Bottom: a cross sectional view of this cavity as well as the electric and magnetic field distributions at characteristic regions.

This strong influence of the accelerating structure leads to a very different RF field distribution than the corresponding waveguide modes. The distribution can be characterized in good approximation in the following way:

– The cylindrical outer wall ($r = R_2$) stays on ground potential; $E\ (r = R_2) \cong 0$; the electric field is concentrated at the accelerating electrodes. Between R_1 und R_2 (Fig. 3) exists only an electric field component $E_\varphi(r)$, with the boundary condition

$$E_\varphi(R_2) = 0 \ . \tag{1}$$

– When integrating along E_φ (see Fig. 3), the induction law leads to the equation

$$\int_{\varphi_1}^{\varphi_2} E_\varphi(r) \cdot r \cdot d\varphi = \frac{d}{dt} \oint_A \vec{B}\, d\vec{A} \ ; \tag{2}$$

where A denotes the segment from r to R_2.

– The magnetic flux density B_z shows a very homogeneous distribution throughout the cavity cross sectional area between R_1 and R_2 (compare the MAFIA result shown in Fig. 4 for half the cross sectional area of a 36 MHz IH-DTL [12]):

$$B_o \cong B_{o,z} \cong const. \quad \text{for} \quad R_1 \leq r \leq R_2 \ . \tag{3}$$

While in empty cylindrical cavities the zero modes H_{mn0} are non-existent [21], they can be realized for the H-structure family discussed here by appropriate shaping of the geometry at the cavity ends (see Fig. 2 and Section 3.1.1).

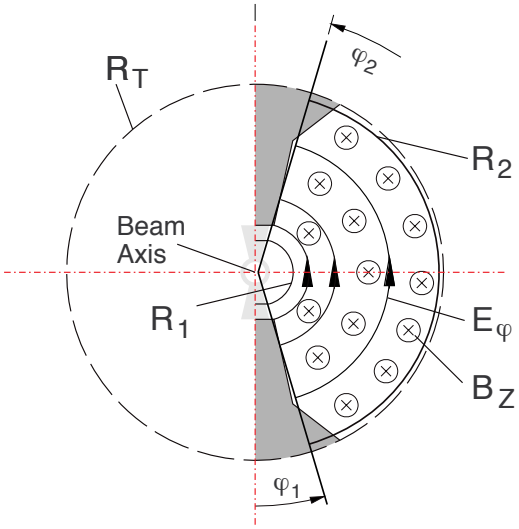

Fig. 3: Approximation of an IH-type structure one-chamber cross section by R_1, R_2, φ_1, φ_2, and field orientation

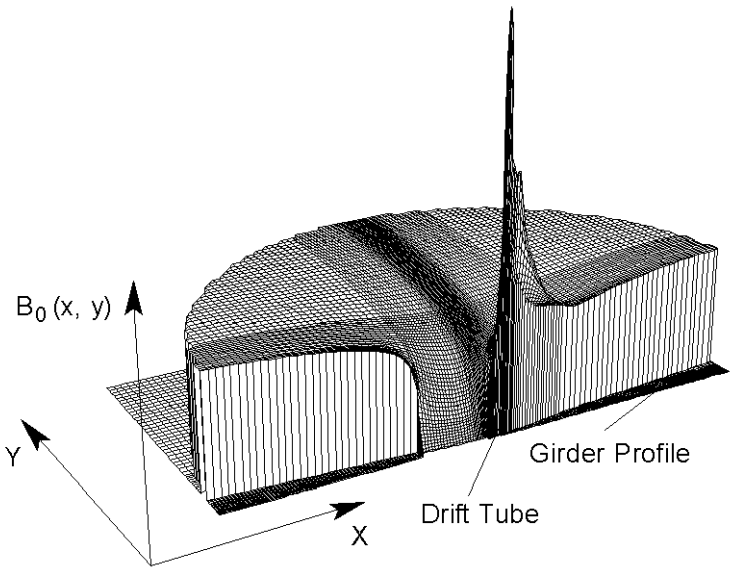

Fig. 4: Magnetic field distribution within one chamber of the 36 MHz IH-DTL, tank 2 of the GSI High Current Linac. The z-coordinate corrresponds to the stem mirror plane of a drift tube connected to the right hand girder. The peak is related to the closed field lines around the stem with conical shape.

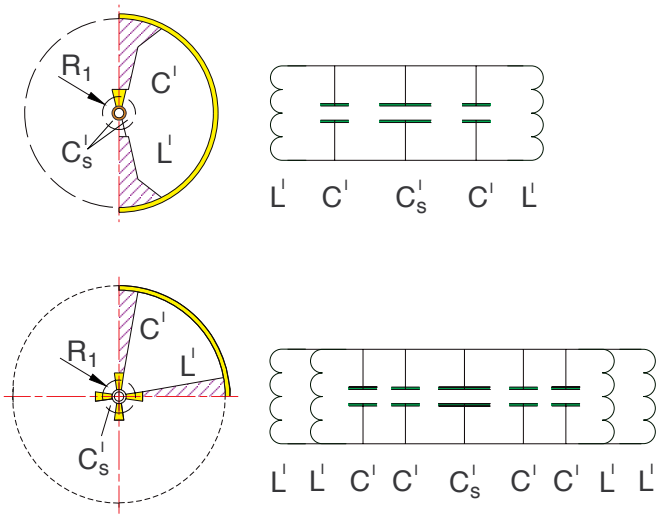

Fig. 5: Equivalent circuits connecting the capacitive and inductive load of one chamber with the corresponding parameters of the whole cavity (H_{110}- and H_{210}-modes)

The main features of H_{mn0}-type linac cavities can now be deduced by investigating the RF field distribution within a slice of the cavity that has unit length. Taking symmetry into account, only half the cross sectional area for H_{11}-modes and a quarter cross sectional area for H_{21}-modes needs to be considered. The resulting parameters can be related to the complete cavity using the simple lumped circuit schemes shown in Fig. 5.

We first divide the tank chamber into two parts. The segment with $< R_1$ is treated separately at the end of the process and refers to the accelerating electrodes and (partially) to the stems. The segment with $R_1 \le r \le R_2$ and $\varphi_1 \le \varphi \le \varphi_2$ is an approximation to the real geometry (see Fig. 4).

We next calculate $E\varphi(r)$. The RF field components are described by

$$E_{\varphi}(r,t) = E_0(r) \cdot e^{i\omega t}; \qquad B_z(t) = B_0 \cdot e^{i\left(\frac{\pi}{2} + \omega t\right)} \quad . \tag{4}$$

Eq. (2) with

$$\Phi(r,t) = B_z(t) \cdot \int_r^{R_2} \int_{\varphi_1}^{\varphi_2} r_1 dr_1 d\varphi \tag{5a}$$

results in

$$-\dot{\Phi}(r,t) = -i\omega\, B_z(t)\ \ (R_2^{\,2} - r^2)\ \ (\varphi_2 - \varphi_1)/2\,. \tag{5b}$$

The corresponding voltage is given by the integral

$$U_i(r) = -\dot{\Phi}\,(r,t) = \int_{\varphi_1}^{\varphi_2} E_0(r) \cdot r \cdot d\varphi \quad . \tag{6}$$

Equating gives the result

$$e^{i\omega t} E_0(r) \cdot r \cdot (\varphi_2 - \varphi_1) = e^{i\omega t} \cdot \omega \cdot B_0 \cdot (R_2^{\,2} - r^2)(\varphi_2 - \varphi_1)/2; \tag{7}$$

$$E_0(r) = \frac{\omega\, B_0 (R_2^{\,2} - r^2)}{2\, r} \quad . \tag{8}$$

We next calculate the stored magnetic field energy per chamber unit length,

$$W'_m = \frac{B_0^2}{2\mu_0} \int_{R_1}^{R_2} \int_{\varphi_1}^{\varphi_2} r\, dr\, d\varphi = \frac{B_0^2}{4\mu_0}\left(R_2^{\,2} - R_1^{\,2}\right)\left(\varphi_2 - \varphi_1\right) \; ; \tag{9}$$

and for the electric field

$$W'^{*}_{el} = \frac{\varepsilon_0}{2} \int_{R_1}^{R_2} \int_{\varphi_1}^{\varphi_2} E_0^2(r) \cdot r\, dr\, d\varphi \; ; \tag{10a}$$

$$W'^{*}_{el} = \frac{\varepsilon_0 \omega^2 B_0^2}{8} \left[R_2^{\,4} \left(\ln \frac{R_2}{R_1} - \frac{3}{4} \right) + R_2^{\,2} R_1^{\,2} - \frac{R_1^{\,4}}{4} \right] \left(\varphi_2 - \varphi_1\right) \; . \tag{10b}$$

While the magnetic field energy within r < R_1 can be neglected for the moment, the electric contribution is estimated by assuming a constant field strength $|E_0| = |E_0(R_1)|$ for this volume. Co m-parisons with MAFIA simulations have shown that this method produces good results as soon as the accelerating structure is included, but that it underestimates the corresponding field contribution when no electrodes are mounted.

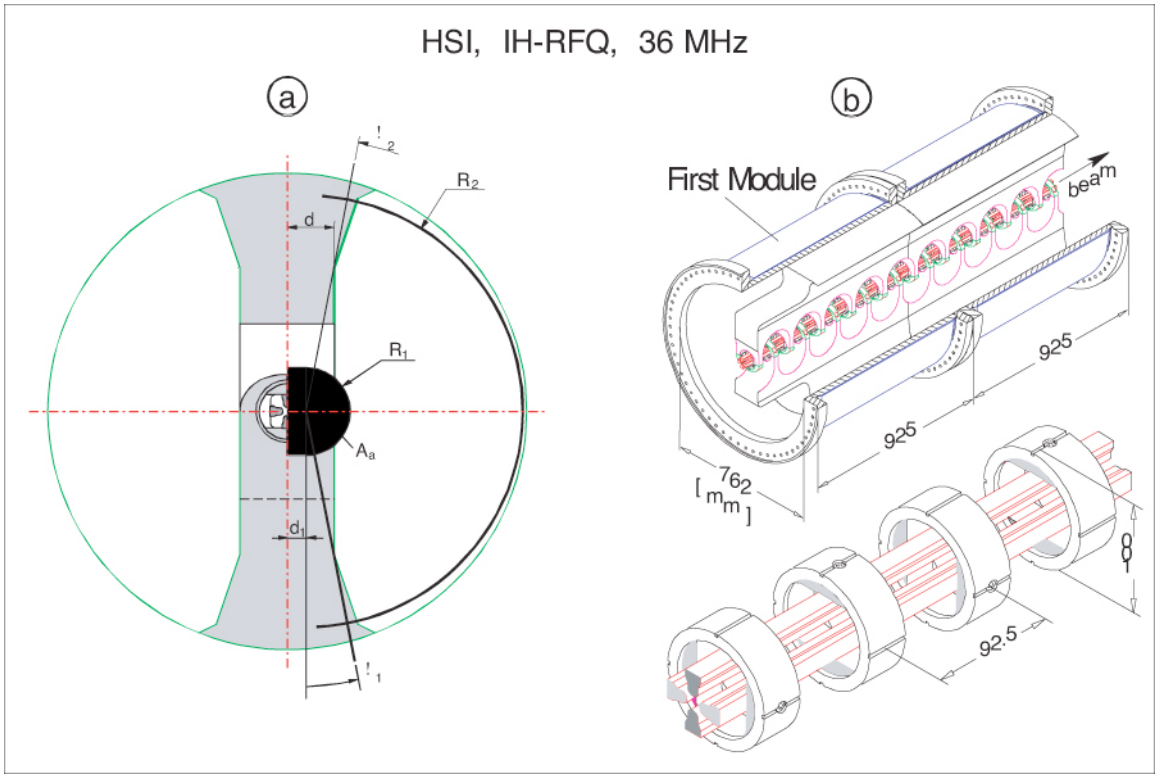

Fig. 6: IH-RFQ: (a) equivalent chamber geometry; (b) the first two of the ten modules from the 9.4 m GSI IH-RFQ, and illustration of the electrodes and carrier rings.

To gain more flexibility in approximating a given cavity geometry, the area within r < R_1 is matched by introducing a factor F (see Fig. 6).

$$A_a = F \cdot \frac{R_1^{\,2}}{2} \cdot \left(\varphi_2 - \varphi_1\right) \; . \tag{11}$$

For the electric field energy, neglecting R_1^4-terms, this finally gives

$$W'_{el} \cong \frac{\varepsilon_o \omega^2 B_o^2}{8} \left[R_2^4 \left(\ln \frac{R_2}{R_1} + \frac{2F-3}{4} \right) + R_2{}^2 R_1{}^2 (1-F) \right] (\varphi_2 - \varphi_1). \tag{12}$$

We can now estimate the resonant frequency of the cavity when the part with $r < R_1$ is omitted. The balance of field energies now leads to the resonance frequency by equating Eqs. (9) and (12):

$$\omega_T = 2c \cdot \left(\frac{R_2{}^2 - R_1{}^2}{R_2{}^4 \left(2 \ln \frac{R_2}{R_1} + \frac{2F-3}{2} \right) + 2 R_2{}^2 R_1{}^2 (1-F)} \right)^{1/2} . \tag{13}$$

It should be noted that ω_T does not depend on $(\varphi_2 - \varphi_1)$. By reducing $(\varphi_2 - \varphi_1)$ the inductivity is decreased in the same way as the capacitance is increased. The capacitive load per unit length fulfils the equation

$$W'_{el} = \frac{1}{2} C' \cdot U_0{}^2 \; ; \quad \text{with} \quad U_o = E_o(R_1) \cdot R_1 \cdot (\varphi_2 - \varphi_1) \; . \tag{14}$$

With Eq. (12) this results in

$$C' = \varepsilon_o \frac{R_2{}^4 \left(\ln \frac{R_2}{R_1} + \frac{2F-3}{4} \right) + R_2{}^2 R_1{}^2 (1-F)}{\left(R_2{}^2 - R_1{}^2 \right)^2 \cdot (\varphi_2 - \varphi_1)} . \tag{15}$$

Including the resonance condition $\omega^2 = (L' \cdot C')^{-1}$, one gets from Eqs. (13) and (15)

$$L' = \frac{\mu_o \left(R_2{}^2 - R_1^2 \right) (\varphi_2 - \varphi_1)}{2} \tag{16}$$

Now follows the calculation of the complete cavity parameters by including the real installations around the beam axis (equivalent magnitudes for the capacitive and inductive load within R_1 are determined). This step has to be done separately for every type of accelerating structure.

The capacitance of so-called mini-vane quadrupoles (Fig. 7) can be estimated by the semi-empirical formula [22]

$$C'_Q / pF/m = \frac{39.37}{\cosh^{-1}((1+R_o/\rho)/\sqrt{2})} + \frac{31.05}{R_o/\rho - 0.414} + 25.28 \ln \left(1 + \frac{h}{a+\rho} \right). \tag{17}$$

In the case of the IH-RFQ, the stem structure leads to an additional capacitive load (see Section 2.1.2).

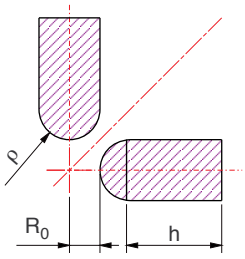

Fig. 7: Illustration of the main parameters defining a mini-vane array

For drift tube structures with diameter ratios $\varnothing_a / \varnothing_i > 1.5$ a semi-empirical formula for calculating the capacitive load is given by Ref. [23]. As H-type DTLs profit significantly from minimizing $\varnothing_a$, the recommended range is $\varnothing_a / \varnothing_i \leq 1.4$ for that geometry—including the dipole field correction in the case of IH-structures (Section 3.4)—and the following concept is useful:

The capacitance of a massive cylinder with radius r_a and length d_e, shielded by two parallel, conducting planes with distance $g_e/2$ is given in good approximation [24] by

$$C^* \approx \frac{2 \cdot \varepsilon_o \pi \, r_a^2}{g_e} \left[2 + \frac{4 \, g_e}{\pi \, r_a} \left(\ln 2 + F_d(x) \right) \right], \tag{18}$$

where F_d is defined by Eq. (19a).

When the shielding planes are positioned in the gap centres, the mirror images produce the neighbouring cell (Fig. 8). The gap voltage is twice the voltage between tube and shielding plane, therefore the capacitance of two $\beta\lambda/2$-cells with $\beta\lambda = 2\,(g + d)$ corresponds to $C^*/2$.

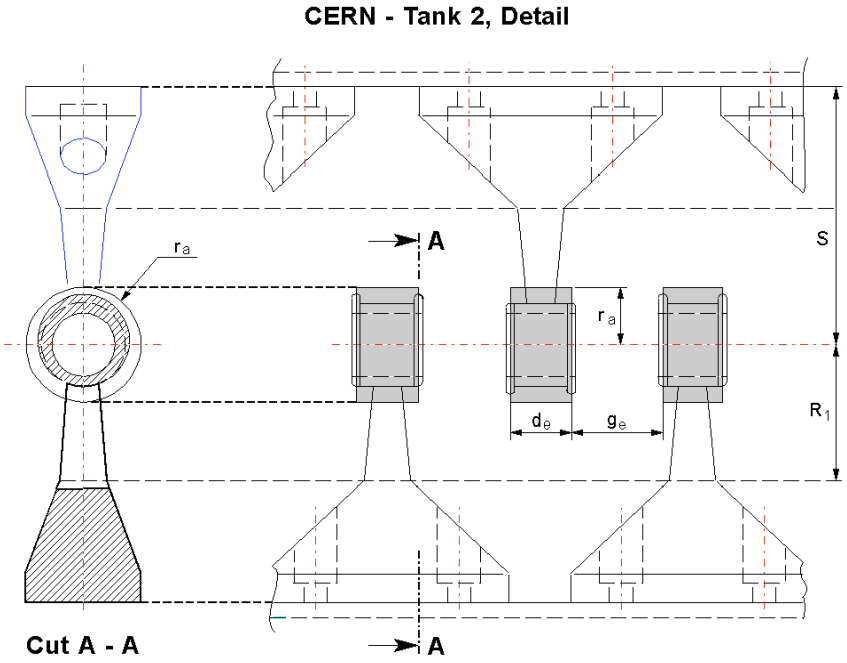

Fig. 8: IH-type drift tube structure and equivalent geometry to calculate capacitive load

The capacitive load per unit length of the drift tube structure results in

$$C'_D = \frac{\varepsilon_0 \pi r_a^2}{2g_e(g+d)} \left[2 + \frac{4g_e}{\pi r_a} \left(\ln 2 + F_d(x) \right) \right] ; \tag{19}$$

with

$$F_d(x) = (1+x)\ln(1+x) - x \ln x \; ; \quad x = \frac{d_e}{2g_e} \; . \tag{19a}$$

The following examples will demonstrate the application of this formalism to realized H-cavities.

2.1.1 Four-vane RFQ (H_{210})

The modulated vane tips are treated by Eq. (17), see also Fig. 9 for an image of the RFQ. To reduce the stray field contribution h = 0 is used. As the total capacitance for r < R_1 is included in this geometry one has additionally to insert F = 0. The cavity parameters are then given by

$$C'_{4Vane} = 4C' + C'_Q \; ; \tag{20}$$

$$L'_{4Vane} = \frac{L'}{4} \cdot \left(\frac{R_2^{\,2}}{R_2^{\,2} - R_1^{\,2}} \right) ; \quad \text{and} \tag{21}$$

$$\omega_{4Vane} = \omega_T \cdot \left(\frac{4C'}{4C' + C'_Q} \right)^{1/2} \cdot \left(\frac{R_2^{\,2} - R_1^{\,2}}{R_2^{\,2}} \right)^{1/2} . \tag{22}$$

Good results were obtained when comparing to realized structures with the parameter choice

$$R_1 \cong 2 \cdot (\rho + R_0) \, . \tag{23}$$

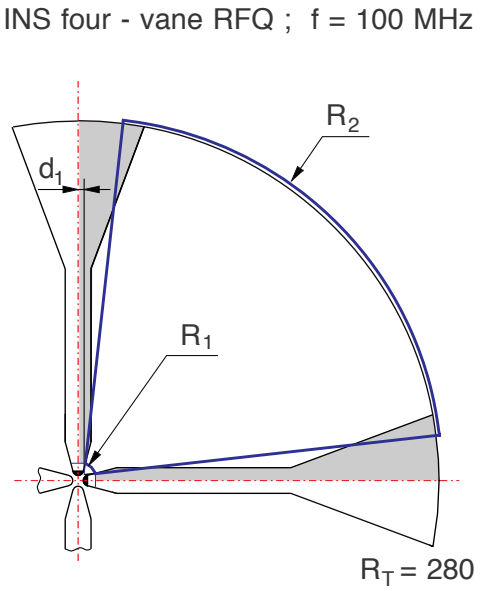

Fig. 9: Equivalent chamber geometry of a four-vane RFQ

2.1.2 IH-RFQ (H_{110})

The mini-vane capacitance is described by Eq. (17). Additionally, the stem structure has to be included. The capacitance C_D between neighboured stems can be estimated by Eq. (19). The contribution C_{QD} between the vane carrier ring and the oppositely charged pair of mini vanes can be deduced by treating each array ring-electrode as a segment of a cylindrical capacitor. Ultimately one gets

$$C'_{IHQ} = 2C' + C'_Q + C'_D + C'_{QD} \; ; \tag{24}$$

$$L'_{IHQ} = \frac{L'}{2} \cdot \left(\frac{R_2{}^2}{R_2{}^2 - R_1{}^2} \right) \; ; \text{and} \tag{25}$$

$$\omega_{IHQ} = \omega_T \cdot \left(\frac{2C'}{2C' + C'_Q + C'_D + C'_{QD}} \right)^{1/2} \cdot \left(\frac{R_2{}^2 - R_1{}^2}{R_2{}^2} \right)^{1/2} \; ; \tag{26}$$

Fig. 6 shows the geometry approximation corresponding to the GSI 36 MHz IH-RFQ [25], as well as a three-dimensional view of two of the ten cavity modules. The individual contributions to the capacitive load of that tank are estimated to be

$$2C' = 11.84\,pF/m \; ; \quad C'_Q = 108.5\,pF/m \; ; \quad C'_D = 43.2\,pF/m \; ; \quad C'_{QD} = 22.9\,pF/m \, .$$

2.1.3 IH-DTL (H_{110})

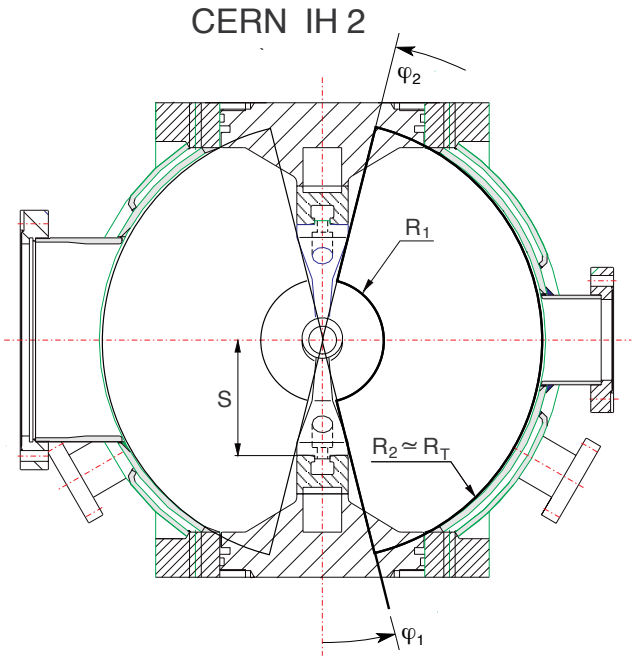

Fig. 10: Equivalent chamber geometry for an IH-DTL

The capacitive load of the drift tubes is estimated by Eq. (19) and the choice of a 'typical' cell geometry for the investigated cavity. The results for the IH-DTL are

$$C'_{IHD} = 2C' + C'_D \; . \tag{27}$$

The capacitance ratios for cavities with slim drift tubes are in the range

$$0.6 < C_D{}' / 2C' < 2.0; \tag{27a}$$

$$L'_{IHD} = \frac{L'}{2} \cdot \left(\frac{R_2{}^2}{R_2{}^2 - R_1{}^2} \right); \tag{28}$$

$$\omega_{IHD} = \omega_T \cdot \left(\frac{2C'}{2C' + C'_D} \right)^{1/2} \cdot \left(\frac{R_2{}^2 - R_1{}^2}{R_2{}^2} \right)^{1/2} . \tag{29}$$

Figure 10 shows an example of a choice of equivalent chamber segment, and Table 1 summarizes parameters for a number of realized cavities.

Table 1: Cavity parameters and measured quantities Z_0, R'_{p0}, Q, with resulting loss factors c_2 for constructed cavities

Machine **H-Type**	**GSI-HLI** **IH-DTL**	**CERN-LINAC 3** **IH-DTL, Tank 2**	**GSI-HSI** **IH, DTL, Tank 2**	**GSI-HSI** **IH-RFQ**	**INS-Tokyo** **four-vane RFQ**
f/MHz	108.4	202.06	36.1	36.1	100
R_2/mm	367	172.5	1017	345	277.4
R_1/mm	60	47.5	120	70	14.6
R_0/mm	–	–	–	5.8	4.1
ρ/mm	–	–	–	4.9	4.1
S/mm	130	90	280	140	–
r_a/mm	16.9	20.2	44	–	–
ϕ_a/mm	24	29	56	–	–
ϕ_i/mm	18	22	46	–	–
Δ/mm	1.5	1.5	5.0	–	–
$\overline{\beta}$	0.045	0.072	0.049	0.0128	0.0137
$Z_0/M\Omega/m$	650	278	390	–	–
$R'_{p0}/k\Omega m$	–	–	–	620	225
Q	20000	12550	39000	13000	11000
N_S	26	14	26.5	–	–
$\sum_j N_{L,j}$	5	0	3	–	–
F_L	0.67	1	0.8	–	–
c_1	1	1	1	1.13	–
c_2	1.47	1.66	1.47	1.31	1.51

2.1.4 CH-DTL

This structure has so far been investigated by MAFIA simulations [26]. Investigations of RF models and prototype cavities are planned in a next step. The corresponding equations for this structure are:

$$C'_{CHD} = 4C' + C'_D; \tag{30}$$

$$L'_{CHD} = \frac{L'}{4} \cdot \left(\frac{{R_2}^2}{{R_2}^2 - {R_1}^2} \right); \text{ and} \tag{31}$$

$$\omega_{CHD} = \omega_T \cdot \left(\frac{4C'}{4C' + C'_D} \right)^{1/2} \cdot \left(\frac{{R_2}^2 - {R_1}^2}{{R_2}^2} \right)^{1/2}. \tag{32}$$

2.2 Acceleration efficiency

The efficiency of drift tube structures is characterized by the resulting effective voltage gain, while the main criterion for RFQs is the achieved vane voltage. As the corresponding parameters are not interpreted in the same way everywhere the used definitions are given by Eqs. (33)–(35) for DTLs and by Eq. (36) for RFQs.

Shunt impedance:

$$Z_0 = \frac{\left(\int_0^l \left| E_{o,z}(z) \right| dz \right)^2}{P \cdot l}; \tag{33}$$

transit time factor:

$$T = \frac{\left| \int_0^l E_{o,z}(z) \cos \omega t(z) dz \right|}{\int_0^l \left| E_{o,z}(z) \right| dz}; \tag{34}$$

effective shunt impedance:

$$Z_{eff} = Z_0 \cdot T^2; \text{ and} \tag{35}$$

specific shunt resistance

$$R'_{p0} = \frac{U_0^2 \cdot l}{P}. \tag{36}$$

The term U_0 denotes the gap voltage and vane voltage amplitude, respectively, while P denotes the RF wall losses. The dimension of Z_0 and Z_{eff} is Ω/m, and R'_p has the dimension Ωm.

The numerical calculation of RF wall losses for complex geometrical structures is not trivial. In addition, contact losses at RF joints and the inclusion of locally enhanced surface current densities along corners etc. are difficult to include. In practice, good results have been obtained by applying the following concept:

– take the parameters from a known cavity of the same type as the one to be calculated;

– derive the equivalent geometrical parameters R_2, R_1, φ_2, φ_1 for both cavities;

– the ratio of shunt impedances between both cavities can then be calculated by using Eq. (50) for DTLs and Eq. (55) for RFQs.

These equations are now derived following in part the concepts of Refs. [5] and [6]. The transversally directed surface current is related to the magnetic field by

$$I_0' = H_o = \frac{1}{\mu_o} \cdot B_o \ . \tag{37}$$

The current path length in the corresponding cavity sector is given by

$$d_I = R_2 \ (\varphi_2 - \varphi_1 + 2c_1) \ . \tag{38}$$

The losses within the region $r < R_1$ are estimated by assuming a homogeneous surface current density from $r = 0$ to $r = R_1$ along virtual surfaces that close the sector under consideration. The value c_1 allows us to regard effective path extensions for 'long' drift tubes and for mini-vanes, and c_1 covers the range

$$1 \le c_1 \le 1.2 \ . \tag{39}$$

The ohmic resistance of a sector length dz is then given by

$$dR \ = \ \frac{R_2(\varphi_2 - \varphi_1 + 2\,c_1)\,c_2}{\kappa \cdot \delta \cdot dz} \ , \tag{40}$$

with skin depth

$$\delta \ = \left(\frac{1}{2} \omega \mu_o \kappa \right)^{-1/2} \ , \tag{41}$$

and a loss coefficient of

$$c_2 = c_c \cdot c_g \ ; \tag{42}$$

where c_c stands for a reduction in conductivity caused by surface quality, tank flanges and RF joints; and c_g allows us to include the additional losses caused by the cavity ends, especially by the girder and vane undercuts, with their high current densities.

The power losses within a cavity sector amount to

$$dP_s \ = \frac{1}{2} \left(I_0' \cdot dz \right)^2 \cdot dR \ ; \tag{43}$$

and with Eqs. (37) and (40)

$$dP_s \ = \frac{1}{2} \left(\varphi_2 - \varphi_1 + 2c_1 \right) c_2 R_2 H_o^2 \left(\frac{\mu_o \omega}{2\kappa} \right)^{1/2} dz \ . \tag{44}$$

The corresponding losses within the complete cavity cross section are given by

$$dP = N_m \cdot dP_s \tag{45}$$

with $N_m = 2$ for H_{11}-cavities and $N_m = 4$ for H_{21}-cavities.

The voltage amplitude is estimated using Eq. (6) with r → 0

$$U_o = \frac{1}{2}\,\mu_o \omega H_o R_2^2\ (\varphi_2 - \varphi_1)\,. \tag{46}$$

Now the shunt impedance and the R'_p value, respectively, can be deduced for all H-type structures discussed here.

2.2.1 Drift tube structures

From Eq. (33) one gets for N_G gaps with gap voltage amplitude U_0 along cavity length l

$$Z_0 = \frac{N_G{}^2 \cdot U_o^2}{P \cdot l}\,. \tag{47}$$

The distance between gap centres corresponds to βλ/2. In non-relativistic approximation one can calculate a velocity parameter β , which is valid for the cavity centre, from given values β_i and β_f at the cavity ends, by the formula

$$\overline{\beta} = \left(\frac{\beta_i^3 + \beta_f^3}{2}\right)^{1/3}\,. \tag{48}$$

It is assumed that the drift tube structure covers the whole cavity length: the number of gaps within l is estimated by

$$N_G \cong \frac{2 \cdot l}{\overline{\beta} \cdot \lambda} = \frac{\omega \cdot l}{\pi \cdot \overline{\beta} \cdot c}\,; \tag{49}$$

Finally, using Eqs. (45)–(49) the shunt impedance results in

$$Z_0 \cong \frac{\mu_o{}^{3/2}\ \kappa^{1/2}\ R_2^3\ (\varphi_2 - \varphi_1)^2\ \omega^{7/2}}{\sqrt{2}\,\pi^2\ c^2 N_m\ (\varphi_2 - \varphi_1 + 2c_1)\,c_2\ \overline{\beta}^2}\,. \tag{50}$$

At a typical operating temperature of 30°C with $\kappa_{Cu} \sim 56 \cdot 10^6\ S/m$ one gets

$$Z_{0,Cu}/\Omega/m \cong 8.4 \cdot 10^{-24}\ \ \frac{R_2{}^3\ (\varphi_2 - \varphi_1)^2 \omega^{7/2}}{N_m \cdot\ (\varphi_2 - \varphi_1 + 2c_1)\ c_2\ \ \overline{\beta}^2}\ \ ; \tag{51}$$

We can now calculate Z_0 exclusively from geometric cavity parameters by including Eqs. (13) and (29) with $N_m = 2$, and Eq. (32) with can be used to calculate ω .

The quality factor of the cavity can be calculated using the definitions

$$P = \frac{\omega\, W}{Q}\,; \qquad P = \frac{N_G^2 \cdot U_0^2}{Z_0 \cdot l}\,; \quad \textit{and} \qquad W = \frac{1}{2}\,C_t^{'} \cdot l \cdot U_0^2\ ;$$

and inserting Eq. (49). The result is

$$Q \cong \frac{\pi^2 \cdot C_t' \cdot Z_0 \cdot \overline{\beta}^{\,2} \cdot c^2}{2\omega}\,. \tag{52}$$

Table 1 (above) shows all relevant parameters for realized structures. By comparing the measured values one gets the following range for the loss coefficient c_2.

$$1.3 \le c_2 \le 1.7 \ . \tag{53}$$

Typical transit time values, Eq. (34), are within the range 0.8–0.84 for an averaged gap/period to length ratio of 0.5. This results in effective shunt impedances

$$0.64 \cdot Z_0 \le Z_{eff} \le 0.70 \cdot Z_0 \ . \tag{54}$$

Acceleration efficiencies of operated IH-structures, including the synchronous RF phase angle Φ_s from the beam dynamics design, are plotted in Fig. 11.

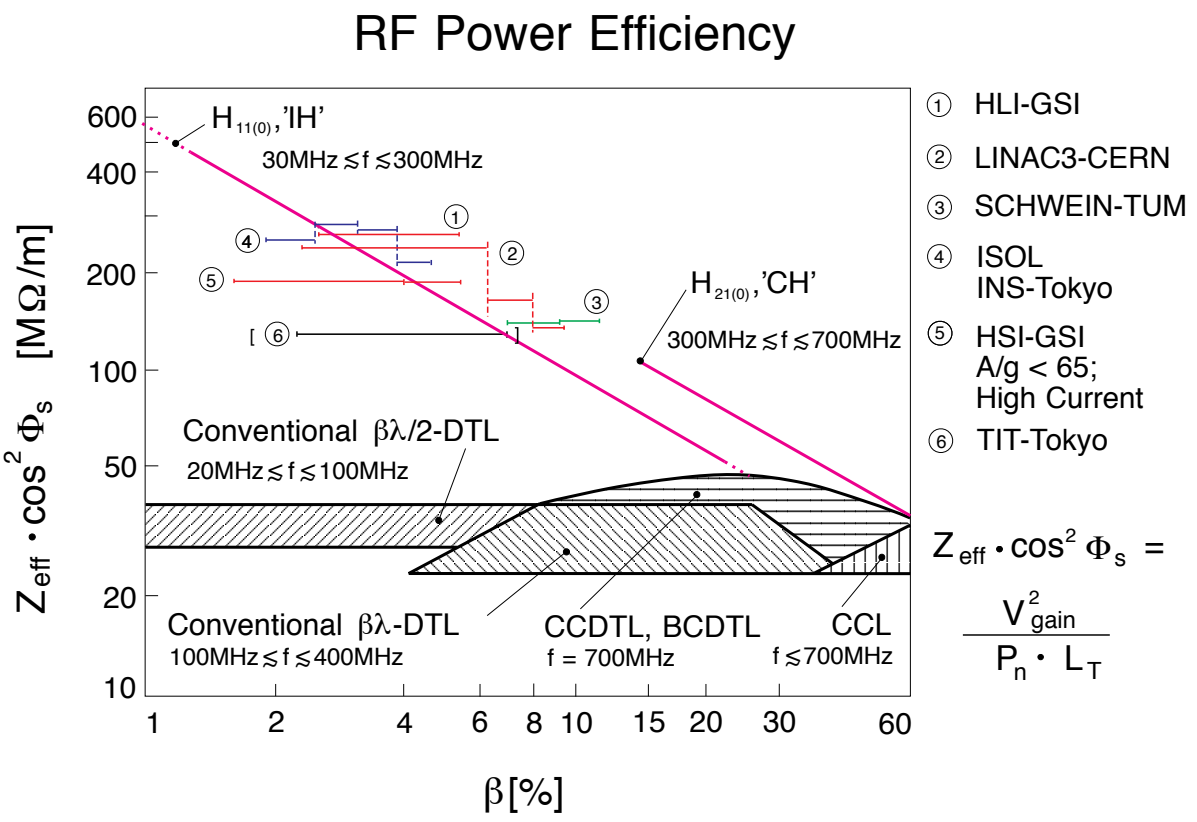

Fig. 11: RF power economy of multicell structures. The advantage of H-type cavities, especially at low beam velocities, is evident. Linacs no. (3) and (4) do not include focusing elements inside the cavities; no. (6) uses conventional beam dynamics (Φ_s = -30°) with quadrupoles in every second drift tube (Φ_a = 100 mm). The 700 MHz CCDTL and BCDTL structures were recently proposed at Los Alamos [27].

2.2.2 RFQ structures

Starting from Eq. (36), R'_{po} is given by

$$R'_{p0} = \frac{\mu_o^{3/2} \kappa^{1/2} R_2^3 (\varphi_2 - \varphi_1)^2 \omega^{3/2}}{\sqrt{2} N_m (\varphi_2 - \varphi_1 + 2c_1) c_2} \ , \tag{55}$$

when inserting Eqs. (44)–(46). Again, using $\kappa_{Cu} \sim 56 \cdot 10^6 \, S/m$ at a typical operating temperature of 30°C, one gets

$$R'_{p0}/\Omega m \;=\; 7.45\cdot 10^{-6}\;\frac{R_2{}^3(\varphi_2-\varphi_1)^2\omega^{3/2}}{N_m(\varphi_2-\varphi_1+c_1)\;c_2}\;. \tag{56}$$

The geometric parameters of the cavity are sufficient to calculate R'_{po} by obtaining ω from Eqs. (13) and (26) with $N_m = 2$ and Eq. (22) with $N_m = 4$, respectively.

The quality factor for RFQs results in

$$Q = \frac{\omega\;C'_t\,R'_{p0}}{2}\;. \tag{57}$$

The parameters of two RFQs that have been constructed are contained in Table 1 (above).

3. DESIGN PRINCIPLES FOR H-CAVITIES

Section 2 explained why a capacitive load reduction of the accelerating structure is especially effective in H-type linacs. This fact has provoked the development of several structure-specific solutions. The examples given here relate to the IH-DTL, but—with the exception of Section 3.4—the concepts can be applied to other H-structures as well.

One main step in the design of efficient H-type DTLs is the application of KONUS beam dynamics to create long, quadrupole-free drift tube sections with small outer drift tube diameters [11–14]. Additionally, a number of specific technical solutions have been developed and are described below.

3.1 Adjustment of the voltage distribution along the cavity

Two powerful concepts are now described that allow the tuning of the cavity with only modest technical effort.

3.1.1 Undercuts

This geometry at the cavity ends (compare Figs. 2 and 12) is most suited to creating the zero mode. The short circuit action of the end walls with respect to H-modes is suppressed by the geometry if the undercuts are large enough.

A lumped circuit equivalent is shown in Fig. 12(a). The centre part of the cavity is represented by C_M and L_M, and the corresponding quantities of one cavity end are denoted by C_E and L_E, and depend on the undercut size. The magnetic field that penetrates the undercuts was measured for a 52-cell IH-DTL in dependence on the window depth L_I (using metallic and dielectric beads [28]).

Figure12(b) shows the conditions for L_I = 60 mm (zero mode) as well as for smaller and larger window sizes. Figure 12(c) plots the magnetic field strength distribution along three paths marked in Fig.12(a) at a fixed window depth.

Figure 13 demonstrates the influence of the undercut depths L_I at the left-hand cavity end on the gap voltage distribution of a 52-cell structure. It becomes obvious that, besides the zero mode, ramped gap voltage distributions can be also be created by this tuning method.

A disadvantage, however, is that considerable RF power is lost with large undercuts because of the high local magnetic surface fields. Therefore many DTL designs prefer to keep the windows below ‘zero mode size’ and to add a second technique for tuning the voltage distribution (described below).

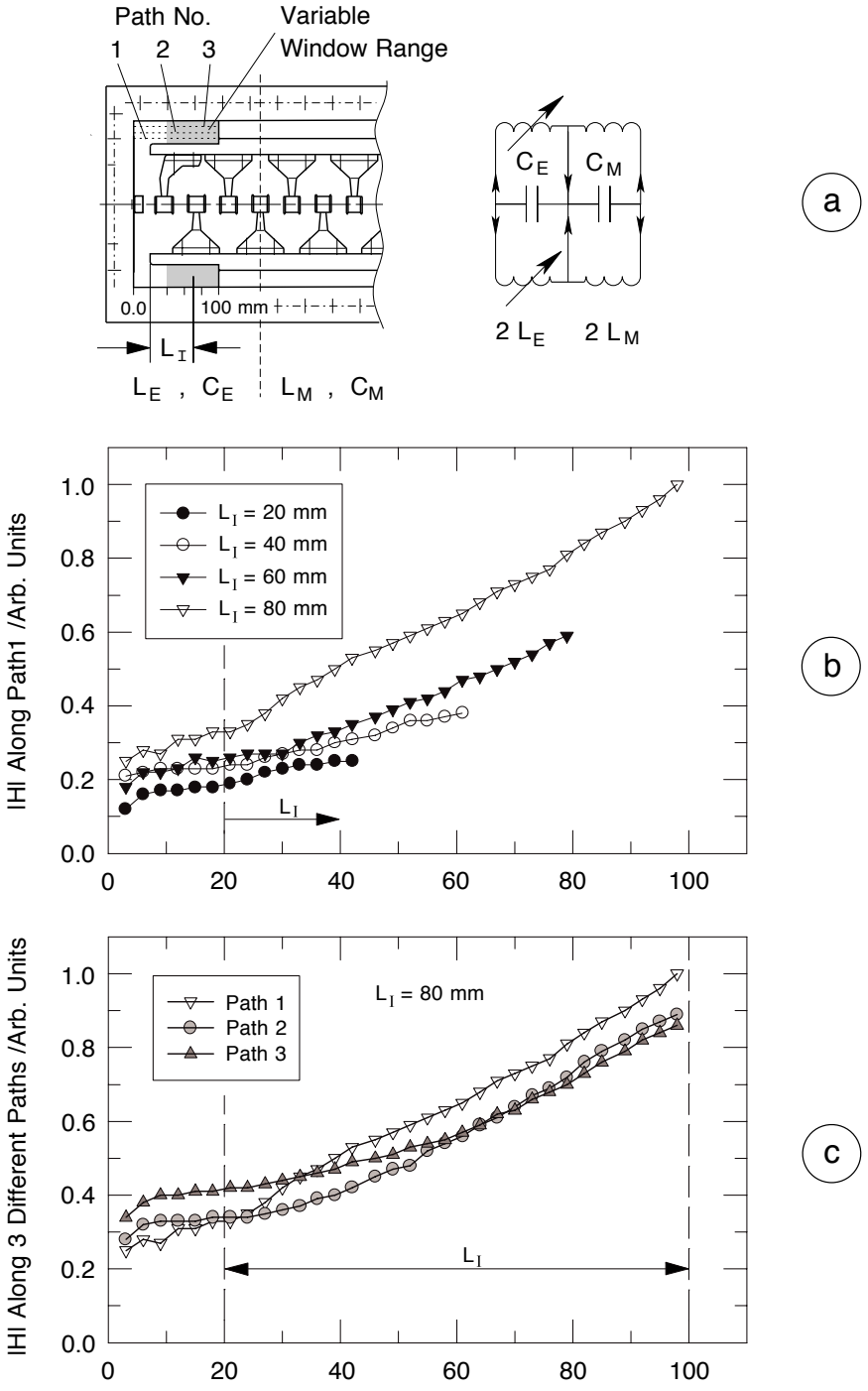

Fig. 12: (a) Functional principle of undercuts; (b) influence of the undercut size on the magnetic field distribution; and (c) field distribution within the undercut cross section for one selected geometry.

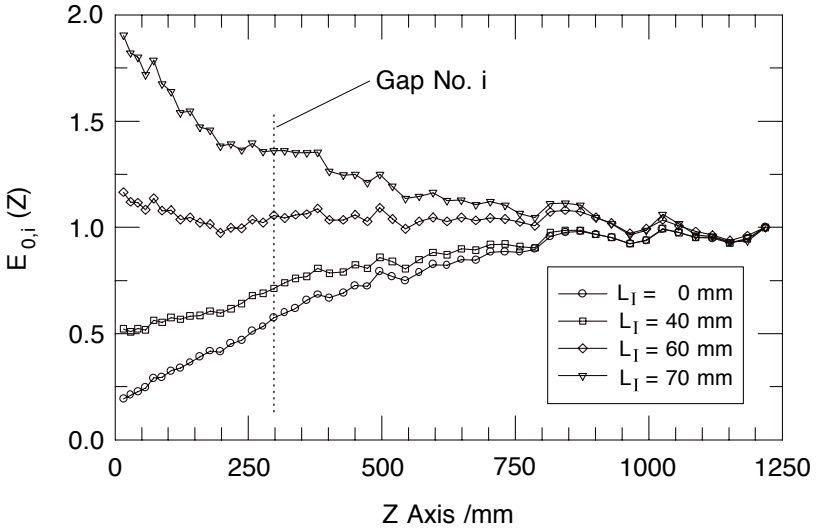

Fig. 13: Variation of the gap voltage distribution along a 52-cell IH-type cavity when changing the undercut depth L_I (see Fig. 12(a)) at the left-hand cavity end. The distributions are normalized at an identical field level in the final gap.

3.1.2 Capacitive load distribution along the drift tube structure

Local gap voltage changes in the range ±20% can be achieved by varying the drift tube geometry along the resonator. The options for this are:

– variation of the gap-to-periodic length ratio;

– variation of the drift tube diameters.

As a consequence one gets a modulation of the capacitive load. To understand the influence on the voltage distribution we start with a zero mode cavity.

Local increase of the drift tube capacitance between z_1 and z_2, with $z_2 - z_1 = l_c$ from the initial value C' to $C'(1+\delta_c)$, results in a change of the cavity frequency

$$\omega_f = \omega_i \left(1 - \frac{\delta_c \cdot l_c}{2 \cdot l_R}\right) . \tag{58}$$

The parameters: charge density, voltage amplitude and surface current, are related by

$$Q'_0(z) = C'(z) \cdot U_0(z) , \tag{59}$$

$$I'_0(z) = \omega \cdot C'(z) \cdot U_0(z) , \text{ and} \tag{60}$$

$$U_0(z) = L' \omega \, I'_o(z) . \tag{61}$$

If one still assumes a constant voltage distribution, the corresponding surface current results in

$$I'_{0,f}(z) = I'_{0,i}(z) \left(1 - \frac{\delta_c \cdot l_c}{2 \cdot l_R}\right) ; \text{ for } z \le z_1 \text{ and } z \ge z_2 ; \tag{62}$$

$$I'_{0,f}(z) \;=\; I'_{0,i}(z)\left(1-\frac{\delta_c \cdot l_c}{2 \cdot l_R}\right)(1+\delta_c);\;\; \text{for} \;\; z_1 < z < z_2\,. \tag{63}$$

This current distribution leads, with Eq. (61), to a voltage increase within l_c:

$$U_{0,f}(z) \;=\; U_{0,i} \;\; \text{for} \;\; z \le z_1 \;\text{and}\; z \ge z_2\,, \tag{64}$$

$$U_{0,f}(z) \;=\; U_{0,i}(1+\delta_c);\;\; \text{for} \;\; z_1 < z < z_2\,, \tag{65}$$

leading to a further current increase in this region, etc.

This simple model explains why the voltage can be increased locally by an increase in the corresponding capacitive load. It can not explain the mechanism quantitatively.

In reality not only transverse, but also longitudinal components of the electric surface currents are induced, as indicated by Fig. 14, which shows that distortions of the capacitive load along a cavity tuned to the H_{110}-mode induce admixtures of $H_{11\ell}$-modes. The most frequently used tuning steps are shown in Fig. 15. Besides the zero-mode needed for RFQs, there is a range of gap voltage distributions indicated in Fig. 15(a), which is used for DTLs in practice. An example of an $H_{11\ell}$ dispersion curve is plotted in Fig. 16.

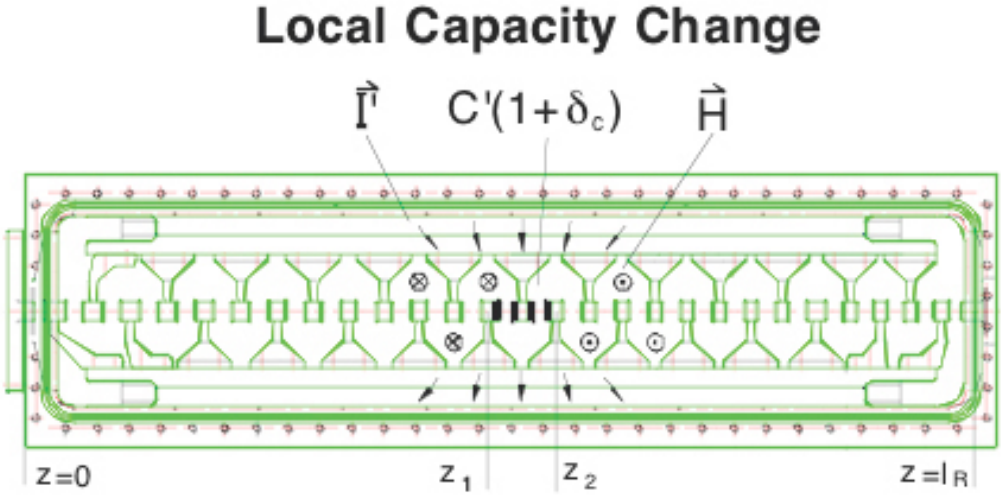

Fig. 14: Electric currents and magnetic field lines induced by increasing the drift tube capacitance locally.

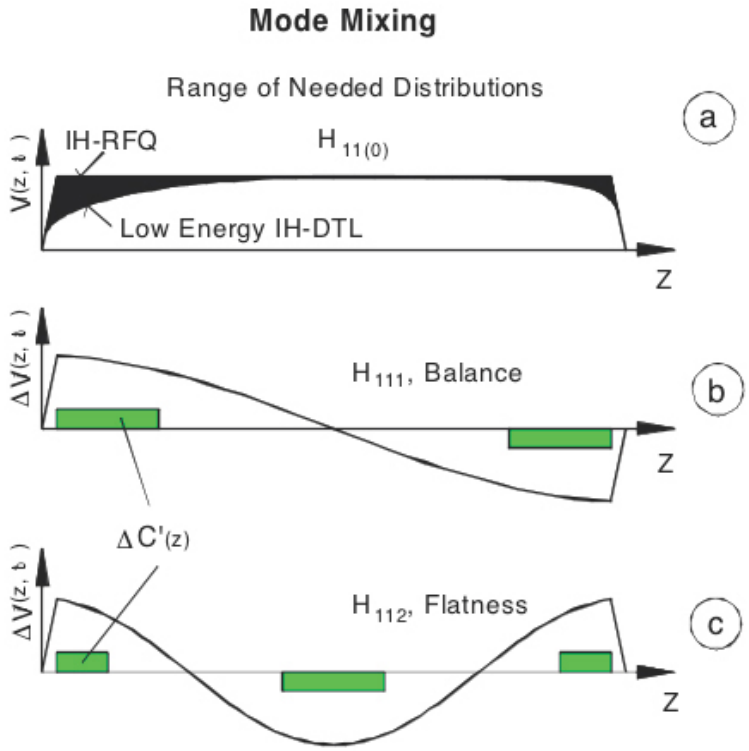

Fig. 15: Top: range of typical voltage distributions along multicell IH-type structures; bottom: superpositioning of $H_{11\ell}$-modes, induced by local variations of the capacitive load.

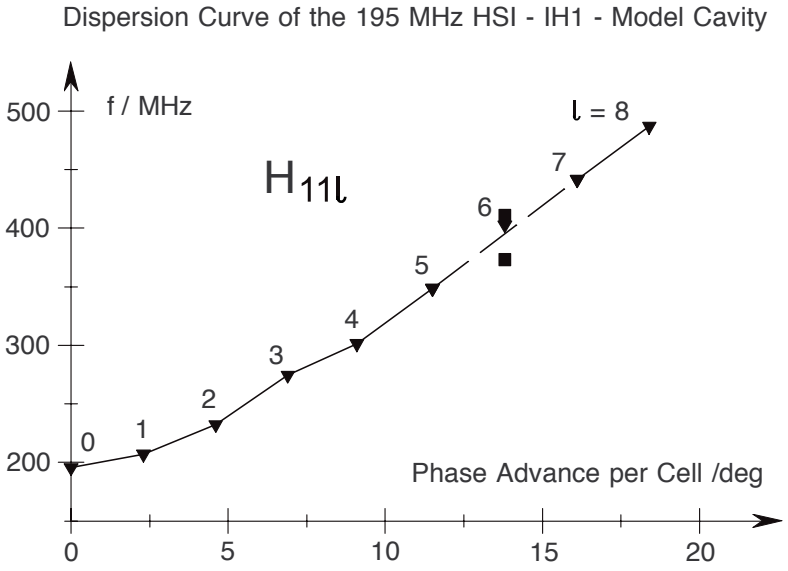

Fig. 16: Measured dispersion diagram for $H_{11\ell}$-modes of a cavity with $\varnothing/l = 0.2$, containing 53 gaps and three triplet lenses.

3.2 Cavity internal lenses

At the DTL front end the voltage amplitude and the corresponding gap number within one KONUS period is relatively small, according to beam dynamics rules. In many cases the resulting geometries correspond to cavity length-to-diameter ratios considerably below 1.0. Such short cavities can be realized. However, the housing of two or more short KONUS periods within one cavity has the following advantages:

– The number of RF amplifier chains required is reduced and the linac cavities can be designed for one RF power class by assigning the corresponding number of KONUS sections to each cavity.

– There is a reduction in low-level RF equipment.

– Simplification of the accelerator structure; short H-cavities are not trivial with respect to RF and mechanical design aspects;

  - intertank sections need some care during design and construction as well as during installation and alignment; and

  - the costs of vacuum equipment for short tanks are higher.

Compared with the advantages mentioned above, the extra efforts involved in housing quadrupole triplets within a cavity are not significant.

Remark: Only if continuous flexibility of the beam energy is needed must one use short cavities. One example of achieving continuous energy variability above 150 keV/u and applying the KONUS beam dynamics is described in Ref. [16].

We now describe two proven concepts for the integration of quadrupole triplets into IH-cavities.

3.2.1 RF-grounded lens housing

At cavity diameters below 1 m and corresponding RF frequencies above 75 MHz, it is desirable to connect the voluminous lens housing to RF ground potential. This allows a match with the capacitive load of the neighbouring drift tube structures. The concept was developed and realized for the 108 MHz High Charge State Injector at GSI [11]. Figure 17 shows the drift tube structure of that cavity as well as a cross sectional cut along the circular stem of one lens, including the adjusting device. The triplet housings are water cooled. The stems are connected to the cavity end by bellows, and the adjusting devices are screwed to the robust main frame. This concept is attractive for cavities with high duty cycle operation, while at low duty cycle the lenses can be connected directly to the cavity without any risk of mechanical displacements during operation.

As the mechanical tolerances of quadrupole lenses are typically ± 0.1 mm, the lens stems should be oriented vertically and point towards the bottom. At the same time the lens is connected to RF ground potential when the accelerating structure is mounted in the horizontal plane (Fig. 17). Matching with the drift tube structure is achieved by the following:

– the distances between girder and lens housing (the left- and right-hand gaps act as series capacitance) cause a capacitive load close to that along the adjacent drift tube structures;

– the two neighbouring drift tubes are at opposite RF potential; RF currents along the lens housing are driven by that array, while the lens stem is transporting no net current if the gap capacities on both sides are equal.

The total length of the j'th lens housing is roughly given by

$$L_{L,j} \cong N_{L,j} \cdot \beta_j \cdot \lambda - \overline{g}_j \quad . \tag{66}$$

The reduction factor of shunt impedance by installing *j* triplet lenses in a cavity, Eq. (50), is given by

$$F_L = \left(1 - \frac{\sum\limits_j N_{L,j}}{N_S}\right)^2 \left(1 - \frac{\sum\limits_j N_{L,j} \cdot \dfrac{R'_S - R'_L}{R'_S}}{N_S}\right)^{-1} . \tag{67}$$

The notation is explained in Appendix A. At moderate tank sizes ($\varnothing \leq 1$ m, $l \leq 4$ m) a well-proven technique is to divide the tank into an upper and a lower shell, plus the centre frame containing the girders as well as the drift tube structure (Fig. 17). Metal sealings are used throughout for all joints (silver, copper, aluminium).

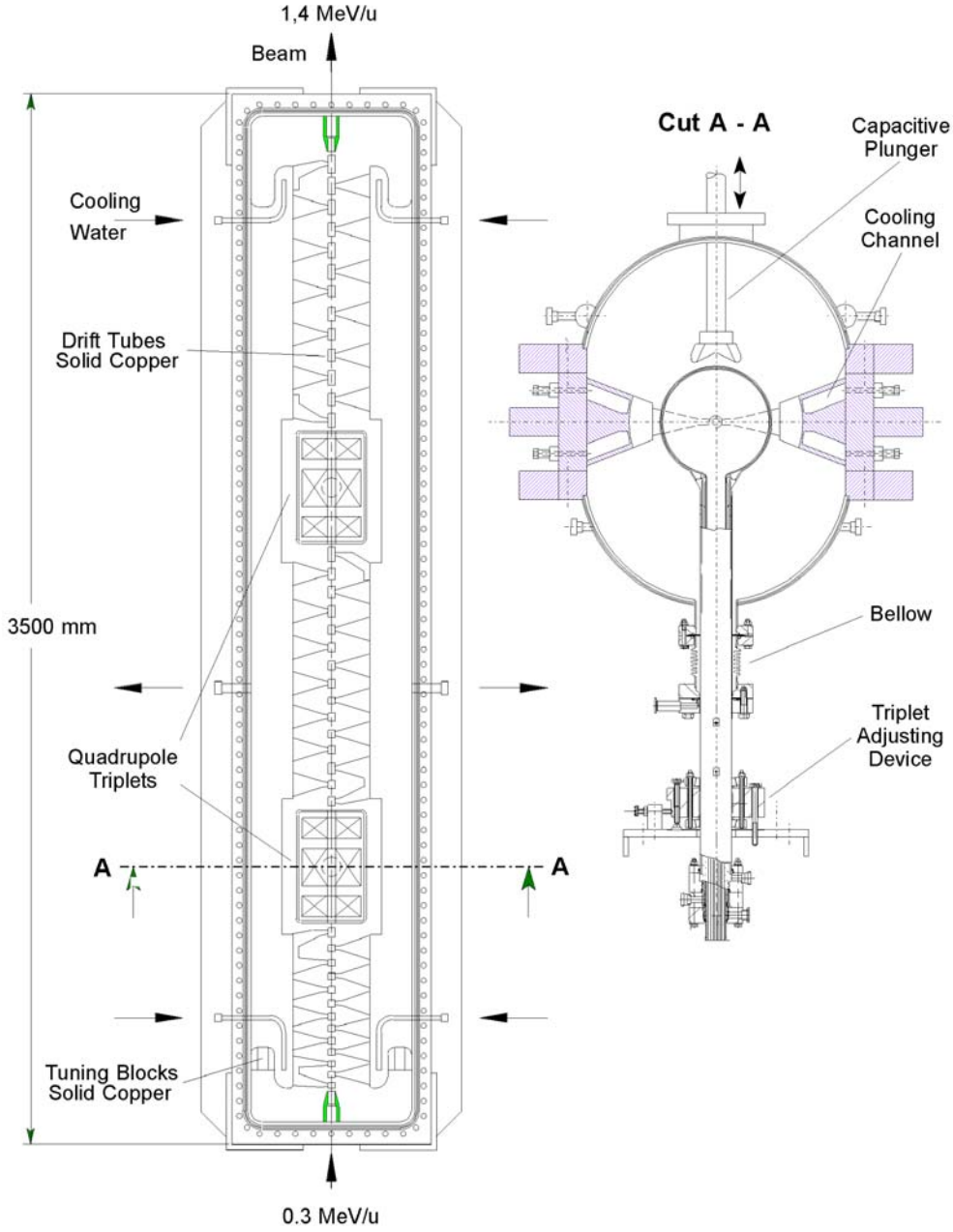

Fig. 17: View of the 108 MHz IH-cavity of the GSI High Charge State Injector containing two quadrupole triplets. Cut A-A shows that the stem causes RF grounding of the corresponding lens housing.

3.2.2 *Lens housing on RF potential*

In the case of large cavity diameters it is preferable to install all accelerating and focusing elements in the vertical plane to achieve sufficient mechanical stability. Moreover, when mounting all lenses of a cavity on top of the bottom girder this girder acts like an optical bench. A flat distribution of the capacitive and inductive load is achieved by creating deep recesses in the top girder and by elongating the lens supports close to the lens ends (Fig. 18). The length of a lens housing j is now roughly given by

$$L_{L,j} = \left(N_{L,j} + \tfrac{1}{2}\right) \beta_j \cdot \lambda - \overline{g}_j \quad , \tag{68}$$

and the shunt impedance when compared to Eq. (50) is reduced by the factor

$$F_L = \left(1 - \frac{\sum_j N_{L,j}}{N_S}\right)^2 \left(1 - \frac{\sum_j \left(N_{L,j} + \frac{1}{2}\right) \frac{R'_S - R'_L}{R'_S}}{N_S}\right)^{-1} \quad . \tag{69}$$

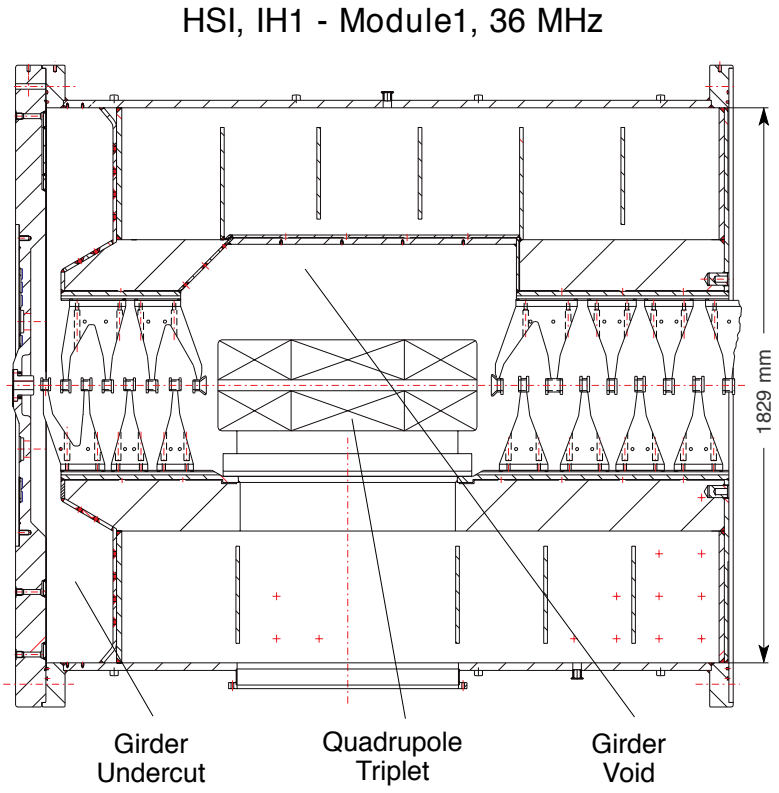

Fig. 18: First module of the 36 MHz High Current IH-DTL, containing one quadrupole triplet mounted on the bottom girder. The pronounced top girder recess is necessary to match the capacitive load.

It should be noted that the length of focusing elements is also an issue if they are mounted outside the cavity. But then the shunt impedance is not affected when the definition as given by Eq. (33) is used.

Each of the two GSI 36 MHz IH-cavities consists of four cylindrical modules, which are bolted together and sealed by aluminum wires. This design is recommended for large tanks.

Remark: The need to integrate lenses into CH-type structures is of less importance as this structure is more often used at higher beam energies. Nonetheless, it is assumed that the concepts described above are applicable to CH-structures as well.

3.3 Electric dipole compensation of the gap fields

IH-type DTLs contain a remaining contribution from the transverse electric field orientation—from stem to stem across each gap. The dipole orientation is inverted from gap to gap and causes either a parallel displacement of the beam or an oscillation around the beam axis (if the beam is injected at an angle relative to the beam axis, or if the voltage of the first and last gap equals just half the voltage of the intermediate gaps).

In non-relativistic approximation the parallel displacement of an axially injected beam after passage of two gaps and of two drift tubes is given by

$$Y = 2\,Y_g + Y_d\,;\ \text{with} \tag{70}$$

$$Y_g \cong \frac{V_{eff}\cdot\cos\Phi\cdot q\cdot tg\delta_{eff}\cdot g}{2m_0c^2\cdot\beta^2}\ ;\ 0.7\,\delta_0 \le \delta_{eff} \le 0.8\,\delta_0\ ;\ \text{and} \tag{71}$$

$$Y_d = d\cdot\alpha(1)\,;\ \alpha(1) \cong \frac{2Y_g}{g}\ ; \tag{72}$$

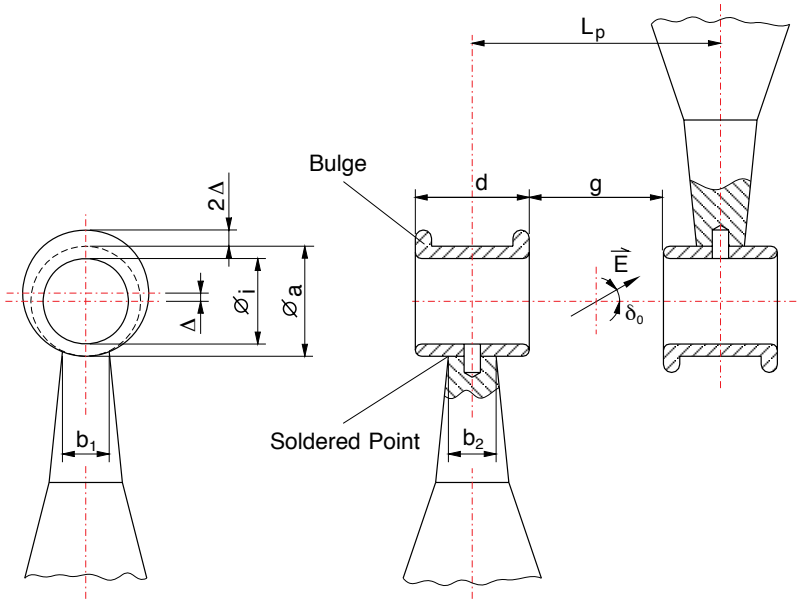

Fig. 19: Drift tube geometry for IH-type structures, reducing the electric dipole content and symmetrizing the field around the beam axis

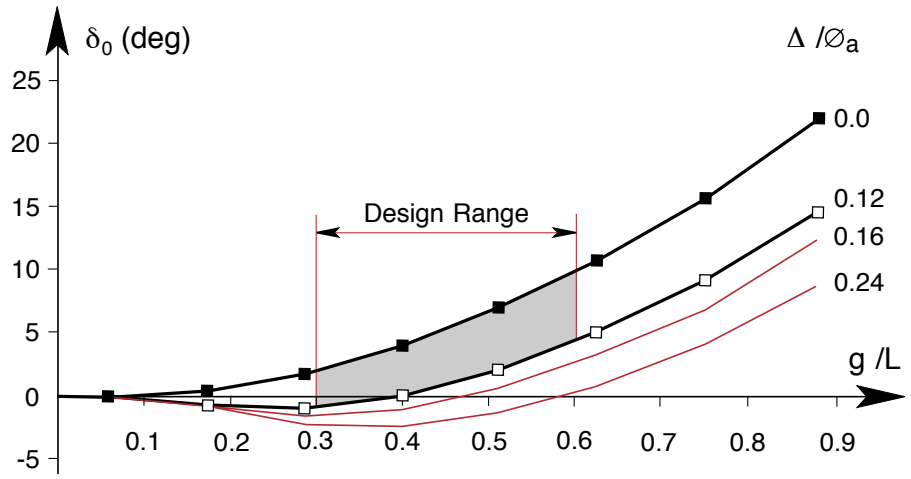

Fig. 20: Angle δ_0 between electric field and beam axis at the gap centre as a function of g/L_p and of the bulge geometry. The plot is valid for the case $\varnothing_a / L_p = 0.48$, $\varnothing_a / \varnothing_i = 1.4$ [29].

Compensation of the dipole component at the low energy end of each linac section corresponding to the same resonance frequency was achieved by developing the drift tube geometry illustrated by Fig. 19. Only at these low energy regions can the conditions

$$g/L_P \leq 0.6\,; \quad \varnothing_a/L_P \geq 0.5 \tag{73}$$

be fulfilled fairly well. Figure 20 shows the δ_0-dependance on the parameters g/L_p and Δ. For the other parts the remaining steering effects have to be investigated, and sufficient steering power within the intertank sections has to be ensured.

A second advantage of the proposed drift tube geometry (Fig. 19) is the improved axial gap field symmetry: the pronounced field maxima within the aperture are shifted radially outwards by the bulges.

3.4 Voltage gain per unit length

The effective voltage gain of an IH-DTL with slim drift tubes as described above is surprisingly high. At the 202 MHz tank 2 of CERN Linac 3 (Fig. 2), an effective voltage gain of up to 10.7 MV/m between end flanges was achieved for 500 μs pulse length and 0.83 Hz repetition rate [30]. Only a few days were available to perform these tests, with voltage levels of up to a factor of 1.82 above the regular operating value (Fig. 21). At the maximum level, about 14% of the RF forward power was absorbed by dark currents. With 1300 kW forward power, 16.5 MV in effective voltage gain were achieved within a total tank length of 1.54 m. Voltage gains of up to around 9 MV/m in the dark current contribution remain in the 1% region. Figure 22 shows MAFIA results for the gap with maximum surface fields. Reasons for the high sparking resistance of the structure when compared, for example, with an Alvarez cavity are assumed to be explained by:

– multipacting at low power levels only (typically in the P ~ 100 W region);

– no high field regions with homogeneous electric field distribution (slim tubes); and

– low stored field energy (modest damages from sparking).

High voltage gains per metre are useful for KONUS structures as they provide sufficient longitudinal focusing power.

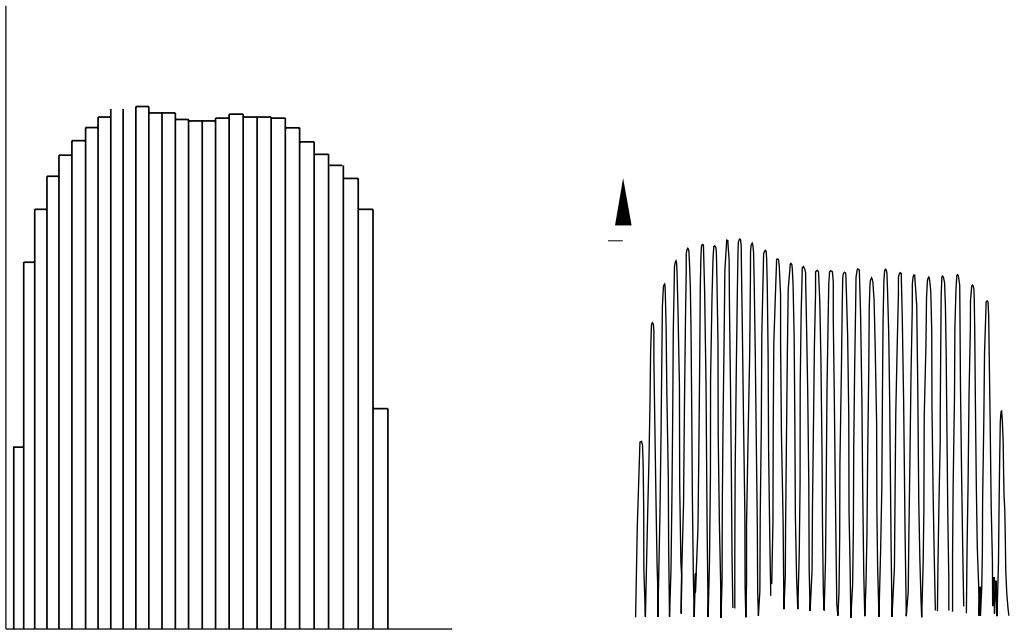

Fig. 21: Gap voltage distribution and on-axis field distribution along the 202 MHz CERN Pb-Linac, tank IH2 (see Fig. 2) at maximum amplitude.

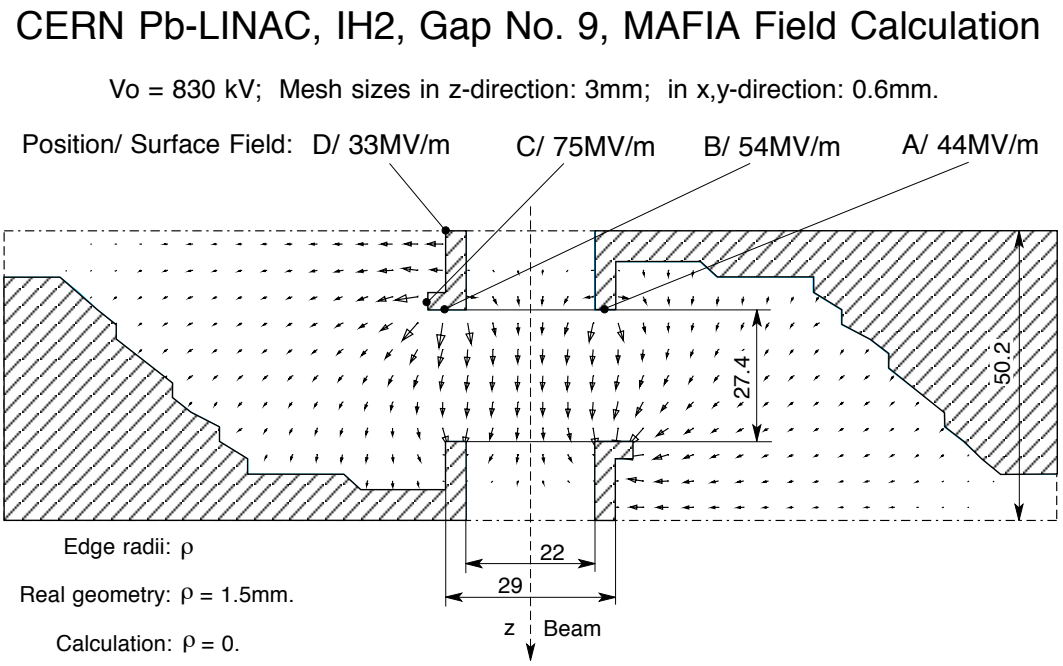

Fig. 22: Calculated electric field distribution at gap no. 9 for the case illustrated in Fig. 21.

4. POTENTIAL OF THE CH-DTL

Analytical estimations and investigations with MAFIA have shown that drift tube structures up to $\beta \leq 0.5$ become accessible with the CH-DTL mode. Operating frequencies can be as high as 700 MHz. A parallel, two-directional investigation is envisaged:

– the development of room temperature prototype cavities; and

– the design and construction of a superconducting prototype cavity [31].

Preliminary beam dynamics investigations with LORASR [32] show that this structure is especially attractive for p and light-ion acceleration including high (100 mA) beam currents. It can be used from the RFQ exit (typically 5–7 MeV/u beam energy) up to injection into a Coupled Cavity Linac (CCL). It is assumed that high voltage gains—similar to IH-DTLs—can be realized. Because of the stem array, no transverse dipole components are contained in the gap field of that structure.

5. CONCLUSIONS

H-type modes are by definition desirable in building RFQs. The IH-RFQ and four-vane RFQ together cover the whole frequency range of interest. By the use of slim drift tubes with adequate stem geometries, matched cavity ends, and application of the KONUS beam dynamics, efficient beam acceleration of up to $\beta \sim 0.25$ by the IH-DTL and $\beta \sim 0.5$ by the CH-DTL can be ahieved. Because of the high capacitive load, the magnetic field distribution becomes very homogenous and realization of the zero mode is possible. These consequences allow for an analytical approach to calculate the RF field distribution.

Three-dimensional codes, together with RF models, are very helpful in the design of H-type structures. Four-vane RFQs were very successful from the beginning. They are the only choice at frequencies above 250 MHz. A number of IH-DTLs are successfully used in routine heavy-ion acceleration operations. The CH-DTL may become the missing link between RFQ and CCL for proton linacs. This structure also provides good mechanical and RF conditions for the development of superconducting CH-cavities.

REFERENCES

[1] P. Blewett, Proc. Symposium in High-Energy Accelerators and Pion Physics, CERN, Geneva, Switzerland, 1956, p. 162.

[2] P.M. Zeidlitz, V.A. Yamnitskii, *J. Nucl. Energy,* **C4** (1962) 121.

[3] V.A. Bomko, E.I. Revutskii, *Sov. Phys. Tech. Phys.* **9** (1965) 973.

[4] M. Bres *et al., IEEE. Trans. Nucl. Sci.* **NS-16/3** (1969) 372.

[5] J. Pottier, *IEEE Trans. Nucl. Sci.* **NS-16/3** (1969) 377.

[6] E. Nolte *et al., Nucl. Instrum. Methods* **158** (1979) 311.

[7] I.M. Kapchinskiy, Proc. LINAC Conf., Seeheim, Germany, 1984, GSI-84-11, p. 43.

[8] J.M. Potter *et al.,* Proc. PAC Conf., San Francisco, USA, 1979, (*IEEE Trans. Nucl. Sci.* **NS-26,** 1979, 3745).

[9] U. Ratzinger *et al., Nucl. Instrum. Methods Phys. Res.* **A263** (1988) 261.

[10] Y. Oguri, E. Arai, T. Hattori, *Nucl. Instrum. Methods Phys. Res.* **A235** (1985) 7.

[11] U. Ratzinger, Proc. LINAC Conf., Newport News, Virginia, USA, 1988, CEBAF–Report–89–001, p. 185.

[12] U. Ratzinger, R. Tiede, *Nucl. Instrum. Methods Phys. Res.* **A415** (1998) 229.

[13] U. Ratzinger, Proc. IEEE Particle Accelerator Conf., San Francisco, USA, 1991, p. 567.

[14] U. Ratzinger, Habilitationsschrift, Goethe-Univ. Frankfurt, 1998.

[15] K. Kaspar, U. Ratzinger, Proc. EPAC Conf., Sitges, Spain, 1996, vol. 3, p. 1973.

[16] R.E. Laxdal, P. Bricault, Proc. LINAC Conf., Geneva, 1996, CERN 96-07, p. 435.

[17] B. Krietenstein *et al.,* Proc. PAC Conf., Vancouver, Canada, 1997, p. 2645.

[18] T. Weis, H. Klein, A. Schempp, Proc. LINAC Conf., Seeheim, Germany, 1984, GSI 84-11, p. 417.

[19] K. Satoh, S. Kamohara, E. Arai, *Nucl. Instrum. Methods Phys. Res.* **A287** (1990) 353.

[20] T.P. Wangler, Proc. LINAC conference, Seeheim, Germany, 1984, GSI-84-11, p. 332.

[21] O. Zinke, H. Brunswig, *Lehrbuch der HF-Technik,* 2nd ed. (Springer-Verlag, 1973).

[22] I. Ben-Zvi *et al.,* Proc. LINAC Conf., Albuquerque, USA, 1990, LA-12004-C, p. 73.

[23] E. Müller and H. Klein, *Nucl. Instrum. Methods Phys. Res.* **A224** (1984) 17.

[24] H. Höft, *Passive elektrische Bauelemente* (Dr. A. Hüthing Verlag, 1977).

[25] U. Ratzinger, K. Kaspar *et al., Nucl. Instrum. Methods Phys. Res.* **A415** (1998) 281.

[26] J.H. Billen *et al.,* Proc. LINAC Conf., Tsukuba, Japan, 1994, p. 341.

[28] R. Popescu-Tiede, diploma thesis, IAP, Goethe Universität Frankfurt, 1993.

[29] J.-C. Nanon, CERN-PS/HI/Technical Note 92-03.

[30] J. Broere *et al.,* Proc. LINAC Conf., Chicago, USA, 1998 ANL-98/28, p. 771.

[31] R. Eichhorn, U. Ratzinger, Proc. 9th Workshop on RF Superconductivity, Santa Fe, USA, 1999.

[32] U. Ratzinger, Proc. GSI Scientific Report, 1998, GSI 99-01, p. 166.

APPENDIX A: DEFINITION OF PARAMETERS

a	aperture radius in RFQs
A	atomic mass number
A_a	geometric area (see Fig. 9(a))
$B, B_0, B_{0,z}$	magnetic flux, amplitude, amplitude of z-comp.
c	velocity of light in vacuum
c_1	loss factor for extra paths along electrodes
c_2	loss factor regarding surface quality, RF joints, cavity ends
C'	capacitance per unit length in one chamber, without electrodes
C'_D	capacitance per unit length of a drift tube structure and of the stems with carrier rings for IH-RFQs, respectively
C'_Q	capacitance per unit length of a quadrupole, consisting of mini vane
C'_{QD}	capacitive contribution 'stems with carrier rings' — 'mini vanes' in IH-RFQs
C'_t	total capacitance per unit length for a cavity
d	drift tube length
d_e	d without rounded ends
d_I	path length of the electric current
$E, E_0, E_{0,z}$	electric field, amplitude, amplitude of z-comp.
f	resonance frequency
F	ratio of geometric areas
F_L	reduction factor of Z_0
g	gap length
$\overline{g}$	average value of two neighbouring gap lengths
g_e	$g + d - d_e$
h	mini vane geometric parameter (see Fig. 6)
H, H_0	magnetic field, amplitude
I	electric current
I'	electric surface current, A/m
$I'_{0,i}, I'_{0,f}$	amplitude of I' before and after a modification
l	cavity length
ℓ	longitudinal mode index
L_I	depth of undercuts (see Fig. 12(a))
L'	chamber inductance per unit of a H-cavity without electrodes
L_L	length of lens housing
L_P	cell length $\beta\cdot\lambda/2$
L_T	tank length between end flanges
m	mode index with respect to φ
n	mode index with respect to r
N_G	gap number of a cavity

$N_{L,j}$	cell number in units of βλ/2 corresponding to the length of lens no. j, including both gap half-lengths
N_S	cavity length in units of βλ/2
P, P'	RF power losses, per unit length
P_s	RF power losses within one resonator chamber
q	ion charge state
Q	quality factor
Q'_0	amplitude of electric charge per unit length
r_a	equivalent outer drift tube radius (see Fig. 8), including the contribution of stems within R_1
R	ohmic resistance
R'_L	ohmic res. per unit length of a cavity at the position of internal lenses
R'_S	ohmic res. per unit length of a cavity along the accelerating sections
R'_{p0}	specific shunt resistance of RFQs, defined by Eq. (36)
R_0	geometric vane parameter (see Fig. 7): averaged aperture radius of a modulated electrode
$R_1, R_2; R_T$	inner and outer radius of the equivalent segment to approximate a cavity chamber cross section; outer chamber radius
T	transit time factor
U, U_0	voltage amplitude
$U_{0,i}, U_{0,f}$	voltage amplitude before and after a modification
Y_g, Y_d	transverse beam excursions in IH-DTLs along gaps and drift tubes
z_0	shunt impedance of DTLs (Eq. 33)
Z_{eff}	effective shunt impedance (Eq. 35)
$\alpha(1)$	deflection angle of the beam caused by a dipole field component after passage of one gap
β	relativistic parameter
$\overline{\beta}$	β-value in the centre of a multicell structure (Eq. 48)
δ	skin depth
δ_C	variation of the capacitive layer
δ_{eff}	reduction of δ_0 when integrating along the whole gap field
δ_0	angle of the electric field direction against the beam axis at the gap centre
Δ	bulge parameter (see Fig. 19)
ε_0	absolute permittivity
κ	electric conductivity
μ_0	absolute permeability
ρ	vane parameter (see Fig. 7)
Φ	magnetic flux
ω	2 π f
ϕ_i, ϕ_a	inner and outer drift tube diameter